Orienting CO molecules with an optimal combination of THz and laser pulses: Optimal control simulation with specified pulse amplitude and fluence

Masataka Yoshida and Yukiyoshi Ohtsuki*
Department of Chemistry, Graduate School of Science, Tohoku University, Sendai 980-8578, Japan
(Received 10 May 2014; published 15 July 2014)

Pulse-amplitude and fluence-specified optimal control simulation with linear (dipole) and nonlinear (polarizability) interactions is applied to find the best way to orient CO molecules with a combination of THz and laser pulses. The optimal pulses are numerically designed with a specified maximum amplitude of the THz pulse and a specified fluence of the laser pulse within the ranges of $E_{\max} = 50$ MV/m ~ 150 MV/m and $f_0 = 2.5$ J/cm^2 ~ 4.5 J/cm^2 at temperature $T = 0$ K ~ 10 K. The optimal pulse almost always consists of a near-single-cycle THz pulse of zero area and a laser pulse that is mainly composed of three subpulses. There is no temporal overlap between the THz pulse and the laser subpulses. The THz pulse, which virtually contains no dc components, induces rotational transitions in a resonant way, whereas the three laser subpulses efficiently induce multiple rotational transitions through Raman scattering. Comparing the optimal control simulations with and without laser pulses, the laser pulses effectively increase the degrees of orientation by approximately half through the polarizability interaction with inversion symmetry.

DOI: 10.1103/PhysRevA.90.013415 PACS number(s): 37.10.Vz, 32.80.Qk, 42.50.Hz

I. INTRODUCTION

In macroscopically isotropic ensembles, such as gases and liquids, the control of molecular alignment or orientation is essential prior to performing molecular-fixed-frame experiments [1], and therefore, it has attracted much attention in the past few decades. As rotational degrees of freedom weakly couple with electric fields, strong fields are required to generate torques to align or orient molecules. To avoid the undesirable effects of such strong fields, molecular alignment or orientation under the field-free condition is desired. In this regard, intense laser pulses are often used to align or orient molecules. When the optical frequency of a laser pulse is much higher than the frequencies associated with rotational transitions, molecules interact with the laser pulse through the cycle-averaged-induced dipole moment [2,3]. Molecular alignment can be achieved by the lowest-order-induced dipole (polarizability) interaction with inversion symmetry. As the alignment control is relatively easy to perform, effective (multipulse) control schemes [4–28] and a wide range of applications that include molecular orbital tomography [29,30], high harmonic generation [31], time-resolved imaging [32], isotope separation [33–35], and reaction dynamics [36–38] have been reported.

On the other hand, research on orientation control under the field-free condition is still in its infancy. The difficulty stems from the requirement of asymmetric interactions. When a phase-locked two-color laser pulse is used to introduce asymmetric interactions through higher-order-induced dipole interactions [39–47], its intensity is usually so high that it may induce undesirable transitions and/or cause damage to molecules. Consequently, we need to utilize permanent dipole moment coupling [48–62] with low-frequency electric fields, such as half-cycle-pulse trains [48] and few-cycle pulses [49–53], to realize molecular orientation in the field-free condition.

A straightforward and effective way is to excite rotational states by using strong THz pulses [49–53]. In fact, according to the recent numerical study by Liao *et al.* [51], quite high degrees of orientation can be achieved by using strong near-single-cycle THz pulses with a maximum amplitude of several GV/m. Although it can be possible to generate such strong THz pulses experimentally [54], the experimental setup for the pulse generation may not be easily manageable in a conventional laboratory.

Alternative approaches that utilize a combination of dipole and low-order-induced dipole interactions have been reported [56–63]. One approach focuses on the combination of half-cycle THz and laser pulses [58,59]. Another approach utilizes a combination of near-single-cycle THz and laser pulses because such a THz pulse with a moderately high intensity is experimentally feasible due to the recent development of THz generation techniques. For example, Kitano *et al.* [60] proposed a two-step scheme that consists of a prelaser pulse and a near-single-cycle THz pulse with a suitable time delay to orient HBr molecules. On the other hand, Shu and Henriksen [61] discussed the roles of half- and single-cycle THz pulses in the presence of a prelaser pulse and showed that the molecular orientation was enhanced due to the quantum interference created by the THz and laser pulses. However, the optimal combination of the two different kinds of electric fields as well as the optimal shapes of the THz and laser pulses is not fully understood.

In the present study, focusing on a case of orientation control of CO molecules, we explore the optimal way to achieve the highest degree of orientation with a combination of THz and laser pulses by means of optimal control simulation [24,64]. To design optimal THz and laser pulses with experimentally feasible specifications and enable semiquantitative analyses, we explicitly specify the maximum amplitude of a THz pulse and the fluence of a laser pulse in the simulation. The values considered here are in the ranges of $E_{\max} = 50$ MV/m ~ 150 MV/m and $f_0 = 2.5$ J/cm^2 ~ 4.5 J/cm^2 at temperature $T = 0$ K ~ 10 K. Within those values, we will show that optimal pulses almost always consist of temporally

*ohtsuki@m.tohoku.ac.jp

 ©2014 American Physical Society

separated near-single-cycle THz pulses of zero area and sets of three laser subpulses. In Sec. II, we summarize the modified optimal control simulation and numerical details. In Sec. III, we show the numerical results and discuss the optimal control mechanisms, and in Sec. IV, we present a summary.

II. OPTIMAL CONTROL SIMULATION

A. Theoretical framework

We consider a rigid-rotor CO molecule with a rotational constant, B. The molecule interacts with a linearly polarized pulse, $\mathbf{E}_{\rm tot}(t)$, given by

$$\mathbf{E}_{\rm tot}(t) = \hat{\mathbf{e}}[E(t) + \varepsilon(t)\cos\omega_L t], \tag{1}$$

where $\hat{\mathbf{e}}$ is the polarization vector, $E(t)$ is a THz pulse, and $\varepsilon(t)$ is the envelope function of a laser pulse with a central frequency, ω_L. If we consider the interaction up to the lowest-order-induced dipole (polarizability) interaction and take the cycle average over the optical frequency, ω_L, the Hamiltonian is expressed as

$$H(t) = B\,\hat{J}^2 - \mu E(t)\cos\theta - \tfrac{1}{4}\alpha(\theta)[\varepsilon(t)]^2, \tag{2}$$

with

$$\alpha(\theta) = (\alpha_\parallel - \alpha_\perp)\cos^2\theta + \alpha_\perp, \tag{3}$$

where $\hat{J}$ is the angular momentum operator, θ is the angle between $\hat{\mathbf{e}}$ and the molecular axis, μ is the dipole moment, and $\alpha_\parallel$ ($\alpha_\perp$) is the polarizability component parallel (perpendicular) to the molecular axis. In Eq. (2), we neglect the THz pulse in the polarizability interaction, provided that the intensity of the THz pulse is not extremely high.

The dynamics of CO molecules is described by the Liouville equation,

$$i\hbar\frac{\partial}{\partial t}\rho(t) = [H(t),\ \rho(t)], \tag{4}$$

where $\rho(t)$ is the density operator. The initial state is given by the Boltzmann distribution

$$\rho^0 = \rho(t=0) = \sum_{J=0}\sum_{M=-J}^{J} |J\,M\rangle p_J(T)\langle J\,M|, \tag{5}$$

where $|J\,M\rangle$ is the eigenstate of $\hat{J}^2$ and $\hat{J}_z$; i.e., $\hat{J}^2|J\,M\rangle = \hbar^2 J(J+1)|J\,M\rangle$ and $\hat{J}_z|J\,M\rangle = \hbar M|J\,M\rangle$. The population of each $|J\,M\rangle$ is given by $p_J(T)$ that is independent of the magnetic quantum number, M.

In optimal control simulation [65,66], a physical objective is specified by a target operator, W. The optimal pulse, which consists of the THz and laser pulses, is defined such that it maximizes the expectation value at a specified final time, t_f. To explicitly specify the maximum amplitude of the THz pulse and the fluence of the laser pulse, we utilize the degrees of freedom originating from the penalty due to the THz pulse energy and that due to the intensity of the laser pulse, respectively. For the latter penalty, we introduce γ to the polarizability such that

$$\alpha(\theta) \to \alpha_\gamma(\theta) = (1+i\gamma)(\alpha_\parallel - \alpha_\perp)\cos^2\theta + \alpha_\perp, \tag{6}$$

where the instantaneous penalty parameter, γ, is a positive function of time [24], although we assume a constant in the present study. It leads to an effective Hamiltonian, $H_\gamma(t)$, in which the polarizability interaction is expressed in terms of $\alpha_\gamma(\theta)$ instead of $\alpha(\theta)$. Because of this, the density operator is replaced by the penalized one, $\rho_\gamma(t)$, the time evolution of which is described by Eq. (4) but with $H_\gamma(t)$ instead of $H(t)$. As the introduction of γ is a numerical technique (penalty), after obtaining the optimal pulses, we substitute them into the original equation of motion, Eq. (4), to calculate the physical properties.

From the above discussion, the functional to be maximized is defined by

$$F[E(t),\ \varepsilon(t)] = \mathrm{Tr}\{W\rho_\gamma(t_f)\} - \int_0^{t_f}\frac{dt}{\hbar A(t)}[E(t)]^2. \tag{7}$$

The second term on the right-hand side represents the penalty due to the THz pulse energy, where the positive function, $A(t)$, weighs the physical significance of the penalty. By applying calculus of variations to Eq. (7) subject to the constraint of the modified equation of motion for $\rho_\gamma(t)$, we obtain the two optimality conditions,

$$E(t) = -\lambda(t)\mathrm{Im}[\mathrm{Tr}\{\,\Xi(t)\mu\cos\theta\,\rho_\gamma(t)\,\}] \tag{8}$$

and

$$\mathrm{Im}[\mathrm{Tr}\{\,\Xi(t)\alpha_\gamma(\theta)\,\rho_\gamma(t)\,\}] = 0. \tag{9}$$

Here we introduce the Lagrange multiplier density, $\Xi(t)$, which obeys

$$i\hbar\frac{\partial}{\partial t}\Xi(t) = [H_\gamma^\dagger(t),\ \Xi(t)] \tag{10}$$

with the final condition, $\Xi(t_f) = W$. Equations (8), (9), and (10) with the modified equation of motion for $\rho_\gamma(t)$ consist of the coupled pulse-design equations.

For numerical convenience, we next rewrite the pulse-design equations in terms of a set of wave functions. To accomplish this, we introduce two time-evolution operators, $U_\gamma(t,0)$ and $V_\gamma(t,0)$, which are defined by

$$U_\gamma(t,0) = \mathcal{T}\exp\left\{-\frac{i}{\hbar}\int_0^t d\tau\,H_\gamma(\tau)\right\} \quad \text{and}$$
$$V_\gamma(t,0) = \mathcal{T}\exp\left\{-\frac{i}{\hbar}\int_0^t d\tau\,H_\gamma^\dagger(\tau)\right\}, \tag{11}$$

with the time-ordering operator, $\mathcal{T}$. Note that $H_\gamma(t)$ is a non-Hermitian operator as it is expressed in terms of $\alpha_\gamma(\theta)$ [Eq. (6)] instead of $\alpha(\theta)$. The operators, $\rho_\gamma(t)$ and $\Xi(t)$, are expressed as

$$\rho_\gamma(t) = U_\gamma(t,0)\rho^0(t)U_\gamma^\dagger(t,0) \quad \text{and}$$
$$\Xi(t) = V_\gamma(t,\,t_f)\,W\,V_\gamma^\dagger(t,\,t_f). \tag{12}$$

If we substitute Eqs. (5) and (12) into Eq. (8), and define

$$|\psi_{JM}(t)\rangle = U_\gamma(t,0)|J\,M\rangle \quad \text{and}$$
$$|\zeta_{JM}(t)\rangle = V_\gamma(t,t_f)W|\psi_{JM}(t_f)\rangle, \tag{13}$$

we have

$$E(t) = -A(t)\mathrm{Im}\sum_{J=0}\sum_{M=-J}^{J} p_J(T)\langle\xi_{JM}(t)|\mu\cos\theta|\psi_{JM}(t)\rangle. \tag{14}$$

To derive Eq. (14), we use the relation

$$U_\gamma^\dagger(t,0) = V_\gamma^{-1}(t,0) = V_\gamma(0,t). \tag{15}$$

Similarly, Eq. (9) is rewritten as

$$\mathrm{Im}\sum_{J=0}\sum_{M=-J}^{J} p_J(T)\,\langle\xi_{JM}(t)|\,\alpha_\gamma(\theta)\,|\psi_{JM}(t)\rangle = 0. \tag{16}$$

In the wave-function formalism, the coupled pulse-design equations are composed of Eqs. (13), (14), and (16).

B. Solution algorithm for pulse-amplitude and fluence-adjusted simulation

For a given set of penalty parameters, $A(t)$ and γ, we solve Eqs. (13), (14), and (16) iteratively by using the monotonically convergent algorithm we developed in our previous study [24,64]. In the algorithm, the square of the pulse envelope, $[\varepsilon(t)]^2$, is rewritten as the product of two identical components, $\varepsilon_1(t)$ and $\varepsilon_2(t)$. Then, the pulse-design equations at the kth iteration step are summarized as follows:

$$i\hbar\frac{\partial}{\partial t}\left|\xi_{JM}^{(k)}(t)\right\rangle = \left\{B\hat{J}^2 - \mu\bar{E}^{(k)}(t)\cos\theta - \frac{1}{4}\alpha_\gamma^\dagger(\theta)\varepsilon_1^{(k)}(t)\varepsilon_2^{(k-1)}(t)\right\}\left|\xi_{JM}^{(k)}(t)\right\rangle, \tag{17}$$

with the final condition, $|\xi_{JM}^{(k)}(t_f)\rangle = W\,|\psi_{JM}^{(k-1)}(t_f)\rangle$, and

$$i\hbar\frac{\partial}{\partial t}\left|\psi_{JM}^{(k)}(t)\right\rangle = \left\{B\hat{J}^2 - \mu E^{(k)}(t)\cos\theta - \frac{1}{4}\alpha_\gamma(\theta)\varepsilon_1^{(k)}(t)\varepsilon_2^{(k)}(t)\right\}\left|\psi_{JM}^{(k)}(t)\right\rangle, \tag{18}$$

with the initial condition, $|\psi_{JM}^{(k)}(0)\rangle = |J\,M\rangle$. The THz pulse and the envelope function of the laser pulse are expressed as

$$\bar{E}^{(k)}(t) = -A(t)\mathrm{Im}\sum_{J=0}\sum_{M=-J}^{J} p_J(T)\left\langle\xi_{JM}^{(k)}(t)\right|\mu\cos\theta\left|\psi_{JM}^{(k-1)}(t)\right\rangle, \tag{19}$$

$$E^{(k)}(t) = -A(t)\mathrm{Im}\sum_{J=0}\sum_{M=-J}^{J} p_J(T)\left\langle\xi_{JM}^{(k)}(t)\right|\mu\cos\theta\left|\psi_{JM}^{(k)}(t)\right\rangle, \tag{20}$$

$$\varepsilon_1^{(k)}(t) - \varepsilon_1^{(k-1)}(t) = -\lambda(t)\mathrm{Im}\sum_{J=0}\sum_{M=-J}^{J} p_J(T)\left\langle\xi_{JM}^{(k)}(t)\right|\alpha_\gamma(\theta)\left|\psi_{JM}^{(k-1)}(t)\right\rangle \times \varepsilon_2^{(k-1)}(t), \tag{21}$$

and

$$\varepsilon_2^{(k)}(t) - \varepsilon_2^{(k-1)}(t) = -\lambda(t)\mathrm{Im}\sum_{J=0}\sum_{M=-J}^{J} p_J(T)\left\langle\xi_{JM}^{(k)}(t)\right|\alpha_\gamma(\theta)\left|\psi_{JM}^{(k)}(t)\right\rangle\varepsilon_1^{(k)}(t), \tag{22}$$

where the positive function, $\lambda(t)$, is a parameter that characterizes the searching speed and accuracy. Note that as shown in Ref. [64], the artificially divided components, $\varepsilon_1^{(k)}(t)$ and $\varepsilon_2^{(k)}(t)$, are proved to converge to the same electric field.

In the present study, the penalty terms are actively utilized to adjust the pulse amplitude and fluence. For this purpose, we introduce the iteration-step dependence into the parameters, $A^{(k)}(t) = A_0^{(k)}\varphi_E(t)$ and $\gamma^{(k)}$, where $\varphi_E(t)$ is an envelope function of the THz pulse (see Sec. IIC). The target values of the maximum amplitude of the THz pulse and the fluence of the laser pulse are set to $E_{\max}$ and f_0, respectively. For the sake of concrete description, we consider the case wherein we obtain $E^{(k)}(t)$ and $\varepsilon_{1,2}^{(k)}(t)$ at the kth iteration step by using the parameters, $A^{(k)}(t)$ and $\gamma^{(k)}$. The maximum amplitude of the THz pulse, $E_{\max}^{(k)}$, and the fluence of the laser pulse, $f^{(k)}$, are calculated by

$$E_{\max}^{(k)} = \max\{|E^{(k)}(t)|\ ,\ \ t\in[0,\,t_f]\} \tag{23}$$

and

$$f^{(k)} = \frac{1}{2}\varepsilon_0\,c\int_0^{t_f} dt\,\varepsilon_1^{(k)}(t)\,\varepsilon_2^{(k)}(t), \tag{24}$$

with the electric permittivity of free space, ε_0, and the velocity of light, c. We then adopt the penalty parameters at the next iteration step according to the following *empirical* relations:

$$A_0^{(k+1)} = \frac{E_{\max}}{E_{\max}^{(k)}}A_0^{(k)} \text{ and } \gamma^{(k+1)} = \left(\frac{f^{(k)}}{f_0}\right)^{1/100}\gamma^{(k)}. \tag{25}$$

The convergence criteria for $E_{\max}^{(k)}$ are given by

$$\frac{\left|E_{\max}^{(k)} - E_{\max}\right|}{E_{\max}} < 10^{-7} \text{ and } \frac{\left|E_{\max}^{(k)} - E_{\max}^{(k-1)}\right|}{E_{\max}^{(k)}} < 10^{-6}, \tag{26}$$

and those for $f^{(k)}$ are given by

$$\frac{|f^{(k)} - f_0|}{f_0} < 5\times10^{-3} \quad \text{and} \quad \frac{|f^{(k)} - f^{(k-1)}|}{f^{(k)}} < 10^{-6}. \tag{27}$$

As regards the functional, $F^{(k)} = F[E^{(k)}(t),\,\varepsilon^{(k)}(t)]$, we evaluate the difference between the functional values at adjacent iteration steps only during the iteration period where the penalty parameters, $A^{(k)}(t)$ and $\gamma^{(k)}$, have constant values, i.e., Eqs. (26) and (27) are satisfied. During the iteration period, we apply the convergence criterion with respect to $F^{(k)}$, which is chosen as

$$F^{(k)} - F^{(k-1)} < 10^{-7}. \tag{28}$$

When all the convergence criteria in Eqs. (26)∼(28) are satisfied at the same time, we regard the pulses as a converged (optimal) solution for a given $\varphi_E(t)$. We will examine how to determine $\varphi_E(t)$ in the next subsection.

C. Numerical details

Here, we summarize the numerical details. The rotational constant is set to $B = 1.92\ \mathrm{cm}^{-1}$, which leads to the rotational period, $T_{\mathrm{rot}} = 8.68$ ps. In the following, time is always measured in units of T_{rot}. The permanent dipole moment has a value of $\mu = 0.057$ a.u., whereas the polarizability has a value of $\alpha_\parallel = 15.63$ a.u. and a value of

$\alpha_\perp = 11.97$ a.u. [67]. The target operator is chosen as a non-negative operator, $W = P\,(1+\cos\theta)P$, where the projector, $P = \sum_{J=0}^{8}\sum_{M=-J}^{J} |J\ M\rangle\langle J\ M|$, is introduced to restrict the rotational states to be optically controlled. The final time is set to $t_f = 2.0$. The equations of motion are numerically integrated by using the 5th-order Runge-Kutta method with the time grid, 10^{-5}.

The initial trial fields of the THz and laser pulses are, respectively, given by

$$E^{(0)}(t) = E_0\,\varphi_E(t)\sin 2\pi\ t \text{ and } \varepsilon_1^{(0)}(t) = \varepsilon_2^{(0)}(t) = \varepsilon_0\,\varphi_\varepsilon(t), \tag{29}$$

where we choose the values of the initial amplitudes, E_0 and ε_0, depending on the target maximum amplitude, $E_{\max}$, and the target fluence, f_0, respectively. As our aim is to design a near-single-cycle THz pulse, we assume the envelope function

$$\varphi_E(t) = \begin{cases} 0 & 0 \leqslant t < t^0_{\rm THz} - 0.5 \\ \cos^2\left[\pi\left(t - t^0_{\rm THz}\right)\right] & t^0_{\rm THz} - 0.5 \leqslant t \leqslant t^0_{\rm THz} + 0.5 \\ 0 & t^0_{\rm THz} + 0.5 < t \leqslant t_f \end{cases}, \tag{30}$$

where $t^0_{\rm THz}$ specifies the temporal peak position. Note that the time interval corresponds to the inverse of the lowest rotational transition, $2B$, so that the envelope function could not impose "strong" constraints on the THz pulse shape. In fact, we sometimes obtain a few-cycle pulse as an optimal solution by using this envelope function (not shown). On the other hand, to minimize the influence of the envelope function on the laser pulse design, we assume a flat-shaped function:

$$\varphi_\varepsilon(t) = \begin{cases} \sin(\pi t/2\tau_L) & 0 \leqslant t < \tau_L \\ 1 & \tau_L \leqslant t \leqslant t_f - \tau_L \\ \sin[\pi(t_f - t)/2\tau_L] & t_f - \tau_L < t \leqslant t_f \end{cases}, \tag{31}$$

where $\tau_L = 0.1$ characterizes the rises of the envelope function.

Finally, we explain how to find the optimal value of $t^0_{\rm THz}$ in Eq. (30), which characterizes the envelope of the THz pulse. We first calculate the optimal pulse with a fixed value of $t^0_{\rm THz} = 1.0$ according to the procedure described in Sec IIB. We then use this converged pulse as an initial guess field to find the optimal value of $t^0_{\rm THz}$. We simply divide the temporal region around $t^0_{\rm THz} \sim 1.0$ with the interval $\Delta t^0_{\rm THz} = 0.01$. With the newly defined $t^0_{\rm THz}$'s, the optimal control simulations are performed to roughly search the maximum value of $\langle\cos\theta\rangle(t_f)$ as a function of $t^0_{\rm THz}$. Each simulation requires typically 10000 iteration steps to meet the convergence criteria. Around the region associated with the turn-over change in the value of $\langle\cos\theta\rangle(t_f)$, we search the optimal value of $t^0_{\rm THz}$ with a smaller interval, $\Delta t^0_{\rm THz} = 0.005$, whereby we find the optimal value of $\langle\cos\theta\rangle(t_f)$ to an accuracy of 2×10^{-3}.

III. RESULTS AND DISCUSSION

Optimal control simulations are performed with sets of specified values, such as the maximum amplitudes of the THz pulse, $E_{\max} = 50$ MV/m ~ 150 MV/m, the fluence of the laser pulse, $f_0 = 2.5$ J/cm^2 ~ 4.5 J/cm^2, and temperature, $T = 0$ K ~ 10 K. As we find that the results share common features, in Sec. IIIA, we focus on one of the examples to discuss the pulse structures and control mechanisms in detail. In Sec. IIIB, we show the results in a systematic way. In the following, we use the terminology "optimal pulse" to mean an optimally designed pulse that is composed of an "optimal THz pulse" and an "optimal laser pulse," and "THz-alone optimal pulse" to mean a THz pulse that is optimally designed without a laser pulse.

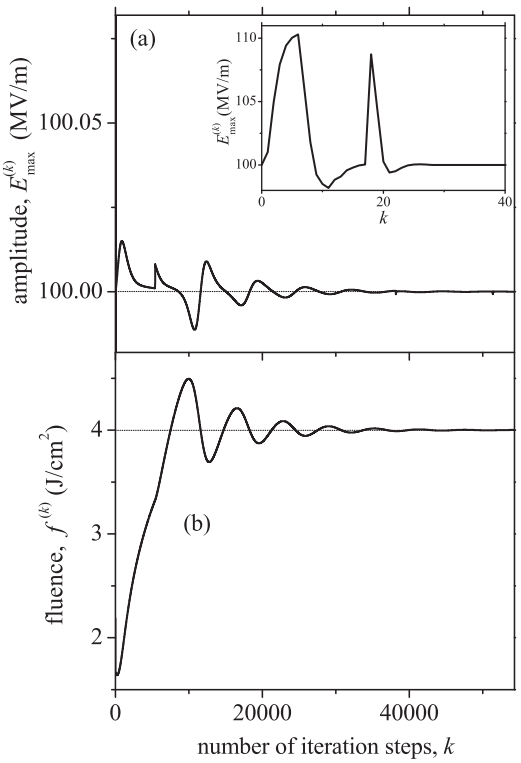

FIG. 1. (a) Convergence behavior of the maximum amplitude of a THz pulse, and (b) that of the fluence of a laser pulse, as a function of the number of iteration steps when the target values are set to $E_{\max} = 100$ MV/m and $f_0 = 4.0$ J/cm^2, respectively. As for the temporal peak of the THz envelope, a fixed value of $t^0_{\rm THz} = 1.0$ is assumed. Inset shows a magnified view of the convergence behavior of the THz pulse amplitude in the first 40 iterations steps.

A. Specific example

As a specific example, we consider the case of $T = 5.0$ K, $E^0_{\max} = 100$ MV/m, and $f_0 = 4.0$ J/cm^2. According to the numerical procedures explained in Sec. IIB, we calculate the optimal pulse by using the initial guess fields [Eq. (29)] with $E_0 = 100$ MV/m and $\varepsilon_0 = 1.0$ GV/m ($f^{(0)} = 2.2$ J/cm^2). The numerical performance is shown in Fig. 1, in which (a) the convergence behavior of the maximum amplitude of the THz pulse and (b) that of the fluence of the laser pulse are shown as a function of the number of iteration steps. In this illustration, the temporal peak of the THz envelope is set to $t^0_{\rm THz} = 1.0$. We see from Fig. 1 that both amplitude and fluence smoothly converge to the specified values after the initial substantial changes ($k \leqslant 100$). The difference in convergence behavior between Figs. 1(a) and 1(b) may stem from the different way

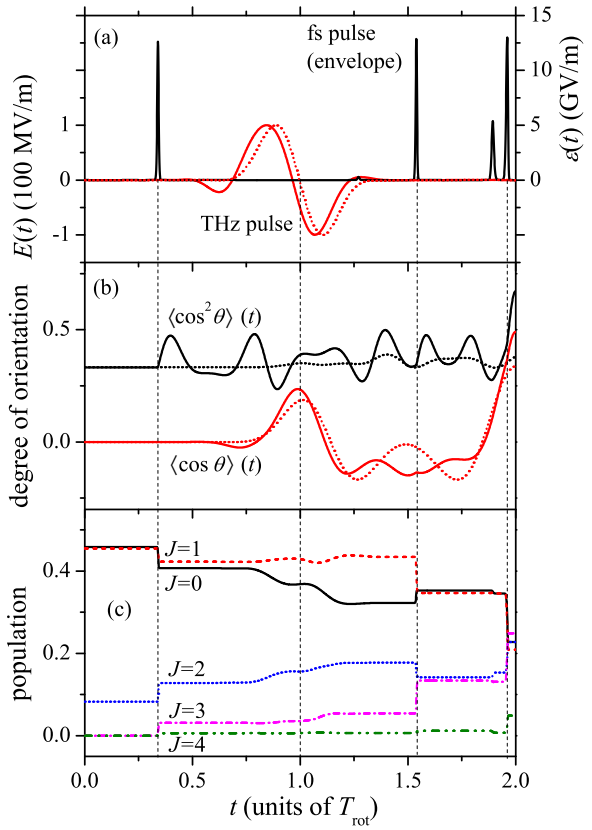

FIG. 2. (Color online) (a) Optimal THz (red solid line) and laser (black solid line) pulses as a function of time. The THz-alone optimal pulse is shown by the red dashed line. Time is measured in units of the rotational period, $T_{\rm rot}$. (b) Time evolution of the degree of orientation, $\langle\cos\theta\rangle(t)$, and that of alignment, $\langle\cos^2\theta\rangle(t)$, are shown by red and black solid lines, respectively. Those induced by the THz-alone optimal pulse are plotted by dashed lines. (c) Time-dependent population of each J state, which is obtained by summing over the populations with magnetic quantum numbers, $M=-J,\ldots,J$.

of updating the penalty parameters [see Eq. (25)] as well as from the different initial guess fields. As explained in the last paragraph of Sec. IIC, starting with this converged pulse, we search the optimal value of $t^0_{\rm THz}$ to obtain the optimal pulse.

The numerical results are summarized in Fig. 2. As shown in Fig. 2(a), the optimal pulse consists of a near-single-cycle THz pulse and three or four laser subpulses. For reference, we also show the THz-alone optimal pulse (dashed line), which is also a near-single-cycle pulse. Note that there is no temporal overlap between the THz pulse and the laser subpulses. This contrasts the advantage of superimposing a laser pulse on a half-cycle pulse [58] to improve orientation control. Figure 2(b) shows the time evolution of the degree of orientation, $\langle\cos\theta\rangle(t)$, and that of alignment, $\langle\cos^2\theta\rangle(t)$. The optimal pulse and the THz-alone optimal pulse (dashed line) lead to $\langle\cos\theta\rangle(t_f)=0.49$ and $\langle\cos\theta\rangle(t_f)=0.33$, respectively. It clearly illustrates the effectiveness of introducing the laser pulse, i.e., the interaction with inversion symmetry can considerably enhance the degree of orientation. By comparing the degrees of alignment, we see that the THz-alone optimal pulse introduces a much smaller change in $\langle\cos^2\theta\rangle(t)$. It is because the THz pulse dominates the $\Delta J=\pm1$ transitions, which slightly enhances $\langle\cos^2\theta\rangle(t)$ through a small shift from the initial thermal equilibrium distribution. Figure 2(c) shows the time-dependent population of each rotational state, which is obtained by summing over the populations with magnetic quantum numbers, $M=-J,\ldots,J$.

First, we consider the structure of the optimal laser pulse in detail. The laser pulse practically consists of three subpulses because the highest degree of orientation decreases by 0.01 when the small subpulse located immediately before the last subpulse is removed. Of the three subpulses, one subpulse appears prior to the THz pulse, which will be referred to as the prepulse, and the other two subpulses appear after the THz pulse, which will be referred to as postpulses. A possible interpretation of the three-subpulse structure can be given according to the frequency-network mechanisms [24]. If we calculate the power spectrum of the envelope function (or the intensity) of the laser pulse (not shown), we see that the major frequency components appear at $5Bn$ ($n=0,\ \pm1,\ \pm2,\cdots$) with sidebands $\pm B$ for $|n|\leqslant2$ and $-B$ for $n\geqslant3$ ($+B$ for $n\leqslant-3$). Those frequency components efficiently induce several lowest Raman transitions (e.g., $10B$ corresponds to the $J=3\leftarrow J=1$ transition), that is, "three" is the minimum number of subpulses to introduce a frequency distribution that is suitable for multiple Raman transitions. If there were only two subpulses, the power spectrum would be composed of equally spaced frequency components, the interval of which would correspond to one of the specific Raman transitions.

In the time domain, we can provide an alternative interpretation by using an analytical expression for the laser-induced excitation process. For illustrative purposes, we restrict ourselves to the $M=0$ (magnetic quantum number) case. As Fig. 2(c) shows that the rotational states up to $J=3$ dominate the dynamics, the wave packet immediately before the interaction, $|\psi_0\rangle$, can be generally expressed as

$$|\psi_0\rangle=\sum_{J=0}^{3}|J\ 0\rangle|\,C_J|e^{-i\,\eta_J}, \tag{32}$$

where $|\,C_J\,|$ and η_J represent the amplitude and the phase, respectively. On the other hand, we see from Fig. 2(a) that the temporal width of each subpulse is much shorter than the rotational period. It means that we can safely neglect the free rotational motion during the polarizability interaction. Dividing the polarizability interaction into the energy shift (Δ) and transition (Λ) parts, we thus have the wave packet immediately after the interaction, $|\psi_+\rangle$,

$$|\psi_+\rangle=e^{i\,\Delta/2}e^{i\,\Lambda}e^{i\,\Delta/2}|\psi_0\rangle, \tag{33}$$

in the second-order split-operator approximation. The operators, Δ and Λ, are expressed as

$$\Delta=\sum_J|J\ 0\rangle\delta_J\langle J\ 0|\quad\text{with}\quad\delta_J=\lambda_{J,J} \tag{34}$$

and

$$\Lambda=\sum_J|J+2\ 0\rangle\lambda_{J+2,J}\langle J\ 0|+\text{H.c.}, \tag{35}$$

where the matrix element is defined by

$$\lambda_{J',J} = \frac{\langle J'\ 0|\alpha(\theta)|J\ 0\rangle}{4\hbar}\int_{-\infty}^{\infty} dt'\,[\varepsilon(t')]^2. \tag{36}$$

By using Eq. (33), we examine the Raman transition effects on the population redistribution among the $J = 0 \sim 3$ states. Expanding Eq. (33) with respect to Λ, we have the populations of the Jth states

$$\begin{aligned} P_{J=2j} &= [1 - 2(\lambda_{2j-2,\,2j})^2 - 2(\lambda_{2j+2,\,2j})^2]|\,C_{2j}|^2 \\ &\quad + (-1)^j 2\lambda_{02}|\,C_0\,||\,C_2\,|\sin(\eta_{20} - \delta_{20}/2) \\ &\quad + (\lambda_{02})^2|C_{2-2j}|^2 + \cdots \end{aligned} \tag{37}$$

and

$$\begin{aligned} P_{J=2j+1} &= [1 - 2(\lambda_{2j-1,\,2j+1})^2 - 2(\lambda_{2j+3,\,2j+1})^2]|\,C_{2j+1}\,|^2 \\ &\quad + (-1)^j \lambda_{13}2|\,C_1\,||\,C_3\,|\sin(\eta_{31} - \delta_{31}/2) \\ &\quad + (\lambda_{13})^2|C_{3-2j}|^2 + \cdots, \end{aligned} \tag{38}$$

where the terms up to the second order in Λ are explicitly shown. In Eqs. (37) and (38), $j = 0,\ 1$, $\lambda_{J,\,J'} = 0$ if $J < 0$ or $J' < 0$, $\delta_{20} = \delta_2 - \delta_0$, $\eta_{20} = \eta_2 - \eta_0$, etc. If the initial state is given by one of the rotational eigenstates, the initial population is simply reduced within the second-order approximation. This situation corresponds to the excitation processes induced by the prepulse. On the other hand, if the initial state is a superposition state, the lowest-order terms of the population redistribution originate from the interference between the wave packet reached by Rayleigh scattering and that by Raman scattering. The interference terms are considerably influenced by the relative phases, η_{20} and η_{31}, immediately before the excitation [Eq. (32)]. For example, if the relative phases are set to $-\delta_{20}/2 + \eta_{20} \approx \pi \pmod{\pi}$ and $-\delta_{31}/2 + \eta_{31} \approx 1.5\pi \pmod{2\pi}$, the populations of the odd-numbered states are selectively excited. This situation roughly corresponds to the first postpulse ($t = 1.54$), at which the populations of the odd-numbered states are more influenced than those of the even-numbered states. If this is so, the relative phases at $t = 1.96$ (second postpulse) are obtained by adding 2.5π and 4.2π to the even- and odd-numbered states, respectively. Those relative phases are suitable for causing both $J = 2 \leftarrow J = 0$ and $J = 3 \leftarrow J = 1$ transitions.

Similarly, we evaluate the time-dependent behavior of $\langle\cos\theta\rangle(t)$. As a minimal analysis, we assume a $J = 0,\ 1$ superposition state as the initial state and consider the terms up to the first order with respect to Λ. The degree of orientation after the laser pulse is applied is expressed as

$$\begin{aligned} &\langle\cos\theta\rangle(t) \\ &\quad = 2\langle 0\ 0|\cos\theta|1\ 0\rangle|\,C_0\,||\,C_1\,|\cos[-2\pi t + \delta_{10} - \eta_{10}] \\ &\qquad + 2\langle 1\ 0|\cos\theta|2\ 0\rangle|\,C_0\,||\,C_1\,|\lambda_{20} \\ &\qquad \times \cos[-4\pi t + (\delta_{21} - \delta_{10} + \pi)/2 + \eta_{10}]\,, \end{aligned} \tag{39}$$

where $\delta_{10} = \delta_1 - \delta_0$, $\eta_{10} = \eta_1 - \eta_0$, etc. Equation (39) indicates the importance of the initial relative phase, η_{10}, when the laser pulse is applied. The condition that the phases of the two cosines are equal to zero can explain the timings of the two postpulses at $t \simeq 1.54$ (1.58) and $t \simeq 1.96$ (1.92) in Fig. 2(a). Here, the values in parentheses are the analytically derived ones. This good agreement, however, does not mean that the present analytic approach can be extended straightforwardly to include more states and/or higher-order contributions of Λ. Such extensions introduce more conditions for the phases associated with the interference terms, thereby resulting in difficulty in finding the "best" values. This situation usually limits the analytic approach to the examination of the pulse structure.

Next, we consider the optimal THz pulse that appears as a near-single-cycle pulse [Fig. 2(a)] with almost zero area. Its peak amplitude is approximately two orders of magnitude smaller than that of the laser pulse, which validates the approximation that the THz pulse makes virtually no contribution to the polarizability interaction [Eq. (2)]. The sine shape means that it does not contain a dc component so that the THz pulse tends to induce resonant transitions between the odd-numbered and even-numbered states. The power spectrum has a central frequency of $3.7B$ (0.21 THz), which is similar to the $J = 2 \leftarrow J = 1$ transition frequency ($4B$). The optimal THz pulse appears slightly earlier than the THz-alone optimal pulse, the latter of which has an optimal value of $t^0_{\rm THz} \simeq 1.0$. Comparing the first peaks between the two THz pulses, the shift is estimated by 0.04, which roughly corresponds to the averaged shift over the two lowest transitions, induced by the two postpulses, $(\delta_{10} + \delta_{21})/2 \times 2 \simeq 0.069\pi$, i.e., 0.035. (The peak intensity and FWHM of each postpulse is estimated as 13.0 GV/m and 44 fs, respectively.) As the energy shifts are virtually independent of the quantum number for $J \geqslant 2$, we expect that such temporal shifts will disappear as the temperature is increased, as will be numerically illustrated later (Fig. 5).

Here we note the relation between the degree of orientation and the sign of the THz pulse. We consider the case wherein the rotational wave packet is described by $|\psi(t)\rangle$. Because the degree of orientation (scalar) does not depend on the choice of the coordinate systems, we have

$$\begin{aligned} \langle\psi(t)|\cos\theta|\psi(t)\rangle &= \langle\bar{\psi}(t)|\cos(\pi - \theta)|\bar{\psi}(t)\rangle \\ &= -\langle\bar{\psi}(t)|\cos\theta|\bar{\psi}(t)\rangle, \end{aligned} \tag{40}$$

where $|\bar{\psi}(t)\rangle$ represents the wave function after the inversion. Under the inversion, the dipole interaction changes its sign such that $-\mu E(t)\cos(\pi - \theta) = \mu E(t)\cos\theta$. That is, $|\bar{\psi}(t)\rangle$ is obtained by applying $-E(t)$ to the initial state $|\bar{\psi}_0\rangle$. If the rotor molecule is initially in the state with no orientation, $|\bar{\psi}_0\rangle$ is the same as the initial state of $|\psi(t)\rangle$ except for a global phase. Therefore, Eq. (40) shows that the degree of orientation changes its sign, $\langle\cos\theta\rangle(t) \to -\langle\cos\theta\rangle(t)$, if we change the sign of the THz pulse, $E(t) \to -E(t)$.

Finally, to visualize the effects of the laser pulse fluence on the control achievement, we numerically design the optimal pulse within $f_0 \in [2.5\ \text{J/cm}^2,\ 4.5\ \text{J/cm}^2]$ at every $0.5\ \text{J/cm}^2$, while assuming a constant value of $E_{\max} = 100\ \text{MV/m}$. Figure 3 shows the optimal degree of orientation as a function of laser pulse fluence. The increase in fluence leads to a monotonic increase in the degree of orientation; however, the change in value is not so large. Scrutinizing the slope, we see that it becomes smaller as f_0 increases, especially around $f_0 = 4.5\ \text{J/cm}^2$. This would suggest that the fluence exerts some kind of saturation effect because only the THz pulse determines the degree of superposition between the

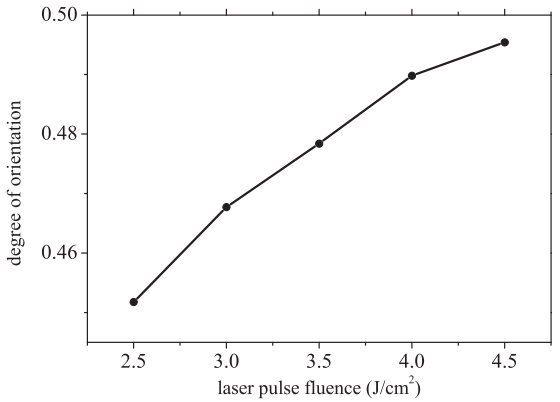

FIG. 3. Optimal degree of orientation as a function of laser pulse fluence. The maximum amplitude of each THz pulse is set to $E_{\max} = 100$ MV/m.

odd- and even-numbered states. As for the laser pulse structure, we observe the following four major features although we do not show the numerical illustrations. (i) The optimal laser pulses always consist of three subpulses. (ii) Their temporal peak positions are independent of the fluence although a smaller fluence leads to slightly less intense and narrower subpulses. (iii) The optimal THz pulses have almost the same shape independent of the laser pulse fluence, although (iv) their temporal peak positions move slightly toward the final time as the fluence decreases, consistent with the laser-induced phase shifts. Those features suggest that the three-subpulse excitation scheme is robust to the fluence range considered here.

B. Effects of temperature and maximum amplitudes of THz pulses

In this subsection, we assume three values of the maximum amplitude of the THz pulse, $E_{\max}$, at $T \in [0\ \text{K}, 10\ \text{K}]$. We show the results by using a set of parameters to see the change in the optimal pulse shape and therefore the control mechanism in a systematic way. In Fig. 4(a), for each specified amplitude of the THz pulse, the degree of orientation achieved by the optimal pulse is plotted as a function of temperature. Within the amplitudes and temperatures considered here, a larger THz amplitude leads to a higher degree of orientation and the degree of orientation decreases as the temperature increases. We have also designed THz-alone optimal pulses with the specified maximum amplitudes, and the degrees of orientation achieved by them are also shown in Fig. 4(a) with dashed lines. By comparing the control achievements with and without laser pulses, we see that the laser pulses considerably improve the degrees of orientation. In fact, from their ratios, which are shown in Fig. 4(b), we see that the combined control typically leads to more than 1.4 times greater degrees of orientation than that without laser pulses. Note that a larger $E_{\max}$ leads to a smaller ratio, which can be partly explained by the fact that the THz pulse with a larger $E_{\max}$ achieves orientation control to some extent even without a laser pulse.

Figure 5 shows the optimal THz and laser pulses (solid lines) and the THz-alone optimal pulses (dashed lines) at $T =$ 3 , 5, 7, and 10 K. We would like to emphasize that in all the cases, near-single-cycle THz pulses are obtained as optimal

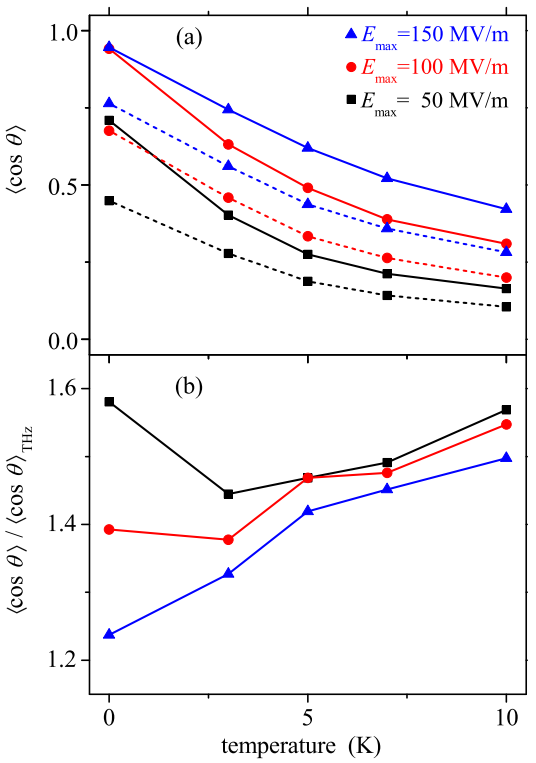

FIG. 4. (Color online) (a) Optimal degree of orientation as a function of temperature, in which the maximum amplitudes of the THz pulses are chosen as $E_{\max} = 50$ MV/m (filled squares), 100 MV/m (filled circles), and 150 MV/m (filled triangles). (a) Values derived by the optimal pulses, $\langle\cos\theta\rangle$, and those by the THz-alone optimal pulses, $\langle\cos\theta\rangle_{\text{THz}}$, are shown by solid and dashed lines, respectively. (b) The ratio of $\langle\cos\theta\rangle/\langle\cos\theta\rangle_{\text{THz}}$ is plotted as a function of temperature for the three different values of $E_{\max}$.

solutions. This is not a trivial result. In fact, we see few-cycle optimal THz pulses in the $T = 0$ K case (not shown). The pulse structures are similar regardless of the maximum amplitude of the THz pulse or the temperature. The laser pulses mainly consist of one prepulse and two postpulses, as indicated by the three vertical dashed lines. We have confirmed that the three main subpulses typically achieve more than 97% of the control. In the worst case at $T = 10$ K, the three subpulses indicated by the vertical dashed lines still achieve 92% of the control.

In addition to the above-mentioned similarities, we see the following four common features. (i) The THz pulses are temporarily shifted toward the final time as the temperature is increased. This can be understood from the fact that a higher temperature leads to more initial populations in the rotational states with higher J numbers, and that the laser-induced energy shifts are virtually independent of the quantum number for $J \geqslant 2$. (ii) The prepulses are also shifted toward the final time as the temperature is increased. This would suggest the importance of the time interval between the prepulse and the THz pulse, that is, the prepulse shifts are accompanied by the THz pulse shifts to keep the time interval between those pulses constant. On the other hand, (iii) the peak positions of the two postpulses are unchanged. This could be understood if the specified final time, $t_f = 2.0$, determines their timings.

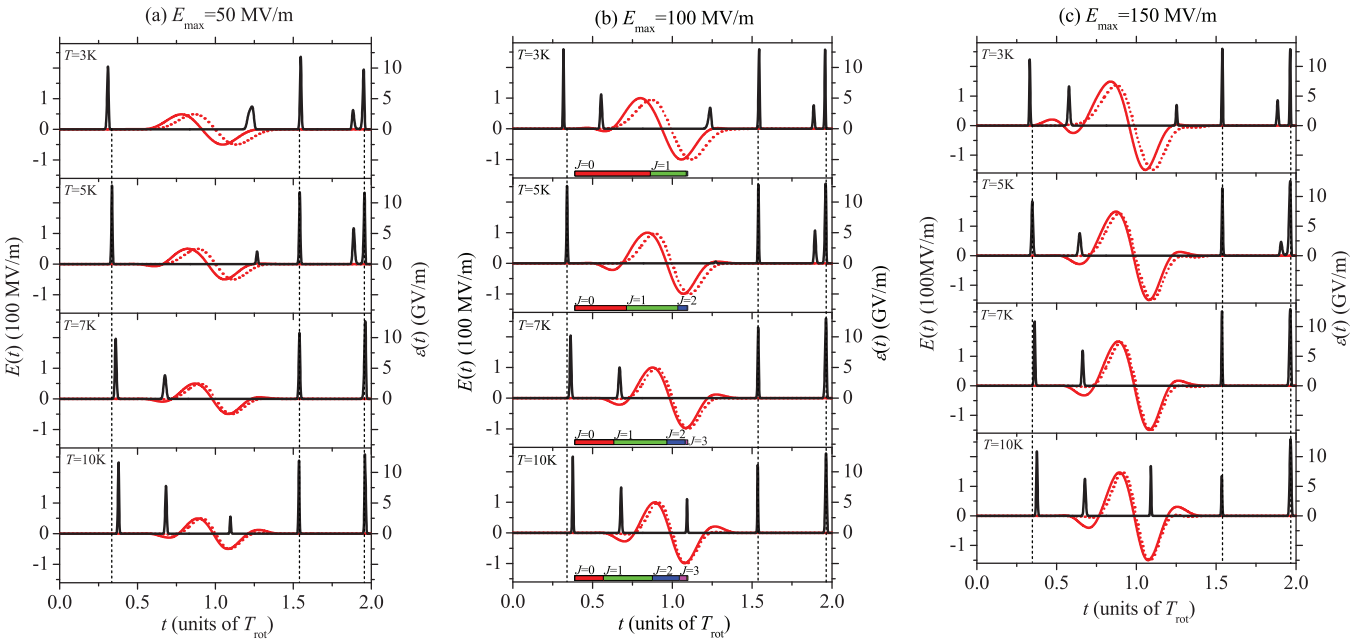

FIG. 5. (Color online) Optimally designed THz (red solid lines) and laser (black solid lines) pulses as a function of time at $T = 3$, 5, 7, and 10 K. The maximum amplitudes of the THz pulses are set to (a) $E_{max} = 50$ MV/m, (b) $E_{max} = 100$ MV/m, and (c) $E_{max} = 150$ MV/m. Left and right ordinates show the scales of the THz and laser pulse amplitudes, respectively. In each figure, the THz-alone optimal pulse is also shown by the red dashed line. The three vertical dashed lines are introduced to indicate the irradiation timings of the three main subpulses. The crossbars in Fig. 5(b) show the initial populations at each temperature.

Actually, when we calculated the optimal pulses by employing three different final times, $t_f = 1.5$, 2.0, and 2.5, without introducing the THz envelope function [Eq. (30)], we found that the last subpulses always appear immediately before the specified final time (not shown). (iv) As shown in Fig. 6, the optimal THz pulses tend to involve higher-frequency components as the temperature and the maximum amplitude, E_{max}, increase. The former is understandable because a higher temperature leads to more thermally excited populations. The latter is explained by the fact that a more intense THz pulse can induce transitions to higher rotational states that have larger transition frequencies.

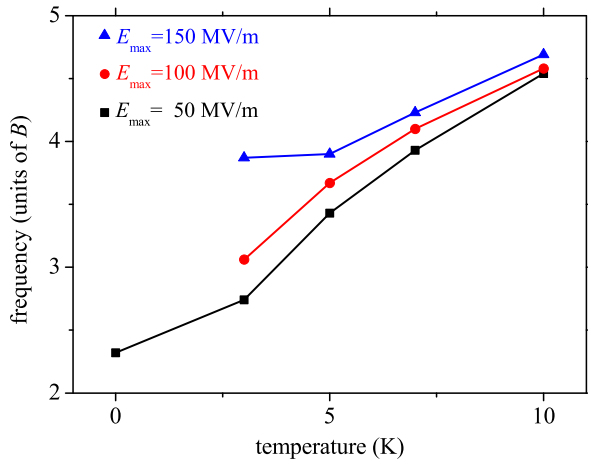

FIG. 6. (Color online) Central frequencies of the optimal THz pulses as a function of temperature, in which the maximum amplitudes are set to $E_{max} = 50$ MV/m (black squares), $E_{max} = 100$ MV/m (red circles), and $E_{max} = 150$ MV/m (blue triangles). In the $E_{max} = 100$ and 150 MV/m cases, there are no data at $T = 0$ K because the THz pulses have double-peak structures so that the central frequencies cannot be determined.

We see from Fig. 5 that the optimal pulses have rather simple structures that could be mimicked by a set of model pulses. Such model calculations can be easily used to evaluate the sensitivity of the pulse irradiation timings. They are also useful to find possible other combinations of pulses that lead to similarly high degrees of orientation. For this purpose, we consider the specific example in Fig. 2, where the optimal THz pulse and the three laser subpulses (envelope functions) can be approximated by

$$E(t) = E_0 \exp\left[-\frac{\left(t - t^0_{\rm THz}\right)^2}{2\sigma^2_{\rm THz}}\right] \sin\omega_{\rm THz}\left(t - t^0_{\rm THz}\right) \quad \text{and}$$

$$\varepsilon_n(t) = \varepsilon_0 \exp\left[-\frac{(t - t_n)^2}{2\sigma^2}\right], \tag{41}$$

with $n = 1,2,3$, respectively, where $|E(t)|_{max} = 100$ MV/m, $\sigma_{\rm THz} = 0.86$, $\omega_{\rm THz} = 3.7\,B$, $\varepsilon_0 = 13$ GV/m, and $\sigma = 3.9 \times 10^{-3}$ (34 fs). The temporal peaks of the envelope functions are specified by $t^0_{\rm THz}$ and t_n ($n = 1$, 2, 3). The total fluence of the laser pulse is set to 4.0 J/cm^2.

As for the pulse irradiation timings, there are three independent parameters that specify the time intervals. For simplicity, we adopt a fixed value of $t_3 - t^0_{\rm THz} = 1.0$, which is determined by the numerical results in Fig. 2(a). We then calculate the maximum absolute values of the degrees of orientation as a function of $t_1 - t^0_{\rm THz} \in [-1.1, 0]$ and $t_2 - t^0_{\rm THz} \in [0, 1.0]$. Note that we search the maximum value for each set of parameters by solving the equation of motion at least one

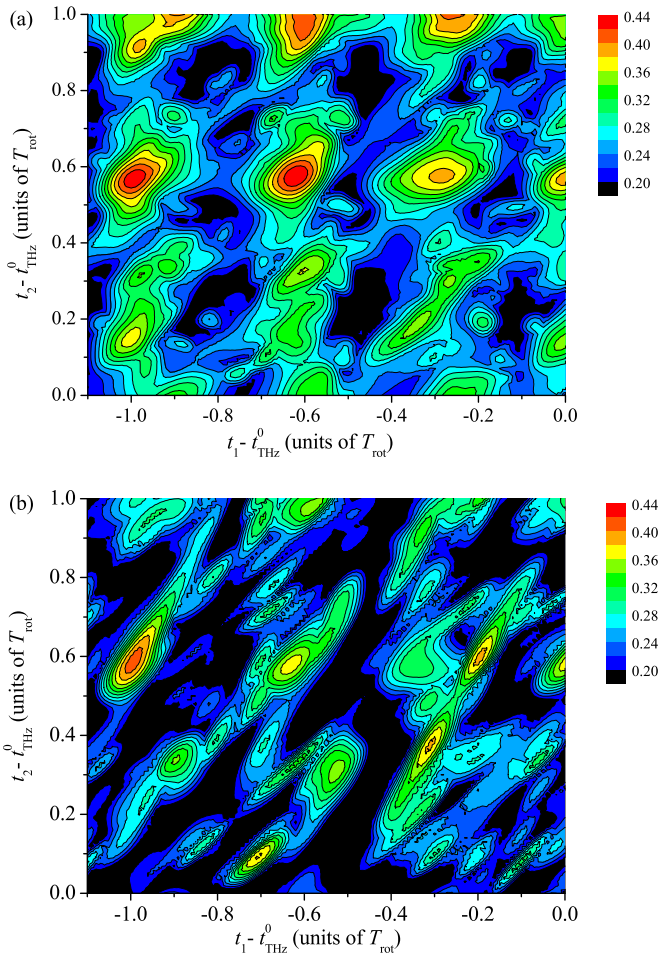

FIG. 7. (Color online) Contour plots of the maximum absolute values of the degrees of orientation as a function of time delays, $t_1 - t^0_{\rm THz}$ and $t_2 - t^0_{\rm THz}$, achieved by sets of model pulses [Eq. (41)] in the (a) three-laser-pulse and (b) two-laser-pulse cases. Here, $t^0_{\rm THz}$ and t_1 and t_2 specify the temporal peaks of the envelope functions of the model THz and laser pulses, respectively. In (a), a fixed value of $t_3 - t^0_{\rm THz} = 1.0$ is assumed.

rotational period after the last subpulse. Figure 7(a) shows the results. There are two regions around $(t_1 - t^0_{\rm THz},\ t_2 - t^0_{\rm THz}) \simeq (-1.0, 0.6)$ and $(-0.6, 0.6)$ that provide quite high degrees of orientation, the latter of which corresponds to the optimal solution. From the region size associated with the optimal solution, the control requires a temporal resolution of $\pm 0.04 \approx \pm 350$ fs to achieve a reasonably high degree of orientation ($\geqslant 0.40$). The other region is located around $(-1.0, 0.6)$ so that the prepulse appears approximately one rotational period before the THz pulse. Its net control time is longer than that of the optimal solution. There are also several regions located around $t_2 - t^0_{\rm THz} \simeq 1.0$ that give reasonably high degrees of orientation. Those regions correspond to two-laser-pulse excitation. Because we do not adjust the amplitudes of the subpulses when there is a temporal overlap between them, the laser pulse fluence associated with those regions is higher than $f_0 = 4.0$ J/cm^2. It may partly explain their high control achievements.

Figure 7(a) could suggest a control scheme that consists of a combination of the near-single-cycle THz pulse and two laser pulses. We numerically evaluate the effectiveness of the scheme by removing the second postpulse. To adopt the same laser pulse fluence as that in Fig. 7(a), we assume $\sqrt{3/2}$ times larger amplitudes for the pre- and postpulses. The maximum absolute values of the degrees of orientation as a function of $t_1 - t^0_{\rm THz}$ and $t_2 - t^0_{\rm THz}$ are contour-plotted in Fig. 7(b). The regions that provide high degrees of orientation significantly decrease compared to those in Fig. 7(a). The values in the regions that correspond to the two-laser-pulse excitation in Fig. 7(a) also significantly decrease. It indicates that the control achievements in those regions are sensitive to the intensities of the pre- and postpulses. This situation is considerably different from the three-subpulse case, in which the control achievements are robust to the total fluence, as shown in Fig. 3.

IV. SUMMARY

We have extended our previous optimal control simulation with nonlinear molecule-electric-field interactions to explicitly specify the pulse amplitude and fluence. The idea is to utilize the flexibility originating from the fluence and instantaneous penalty terms. The simulation has been applied to the orientation control of CO molecules with a combination of a THz pulse and a laser pulse when the maximum amplitude of the THz pulse and the fluence of the laser pulse are, respectively, chosen as $E_{\rm max} = 50 \sim 150$ MV/m and $f_0 = 2.5 \sim 4.5$ J/cm^2 at $T = 0 \sim 10$ K. The systematic analyses clearly illustrate the effectiveness of introducing laser pulses that contribute to the molecular orientation through the polarizability interaction with inversion symmetry. When the THz pulses have the moderately high amplitudes considered here, we explicitly show that near-single-cycle THz pulses can be the optimal solutions in the combined control scheme. Regarding the structures of the THz pulses, they virtually contain no dc components and mainly induce resonant rotational transitions. On the other hand, the optimal laser pulses almost always consist of three subpulses, and the control achievements are weakly dependent on the fluence of the laser pulses. One of the subpulses appears before the THz pulse and the other two appear after it, and there is virtually no temporal overlap between the optimal THz pulse and the laser subpulses. The three laser subpulses lead to network structures in the frequency domain, which could efficiently induce the multiple rotational transitions through Raman scattering.

The present simulations explicitly specify the amplitudes and fluence of the THz and laser pulses within experimentally available values. In addition, the numerically designed pulses have simple structures and the control achievement is weakly dependent on the laser pulse fluence. The present results may serve as a good reference and guide for the further development of orientation control experiments with the combined THz and laser pulses.

ACKNOWLEDGMENTS

We acknowledge stimulating discussions with Professor H. Kono and Professor T. Nakajima. This work was supported

partly by a Grant-in-Aid for Scientific Research, (Grant No. (C) 23550004), and also in part by the Joint Usage/Research Program on Zero-Emission Energy Research, Institute of Advanced Energy, Kyoto University (Grant No. ZE26B-4).

[1] R. N. Zare, *Angular Momentum* (Wiley, New York, 1988).
[2] B. Friedrich and D. Herschbach, Phys. Rev. Lett. **74**, 4623 (1995).
[3] B. Friedrich and D. Herschbach, J. Phys. Chem. **99**, 15686 (1995).
[4] F. Rosca-Pruna and M. J. J. Vrakking, Phys. Rev. Lett. **87**, 153902 (2001).
[5] E. Péronne, M. D. Poulsen, C. Z. Bisgaard, H. Stapelfeldt, and T. Seideman, Phys. Rev. Lett. **91**, 043003 (2003).
[6] M. Leibscher, I. Sh. Averbukh, and H. Rabitz, Phys. Rev. A **69**, 013402 (2004).
[7] J. G. Underwood, B. J. Sussman, and A. Stolow, Phys. Rev. Lett. **94**, 143002 (2005).
[8] M. Renard, E. Hertz, S. Guérin, H. R. Jauslin, B. Lavorel, and O. Faucher, Phys. Rev. A **72**, 025401 (2005).
[9] K. F. Lee, E. A. Shapiro, D. M. Villeneuve, and P. B. Corkum, Phys. Rev. A **73**, 033403 (2006).
[10] K. F. Lee, D. M. Villeneuve, P. B. Corkum, A. Stolow, and J. G. Underwood, Phys. Rev. Lett. **97**, 173001 (2006).
[11] C. Horn, M. Wollenhaupt, M. Krug, T. Baumert, R. de Nalda, and L. Bañares, Phys. Rev. A **73**, 031401(R) (2006).
[12] C. Z. Bisgaard, S. S. Viftrup, and H. Stapelfeldt, Phys. Rev. A **73**, 053410 (2006).
[13] H. Hasegawa and Y. Ohshima, Phys. Rev. A **74**, 061401(R) (2006).
[14] T. Seideman and E. Hamilton, Adv. At. Mol., Opt. Phys. **52**, 289 (2005).
[15] D. Pinkham, K. E. Mooney, and R. R. Jones, Phys. Rev. A **75**, 013422 (2007).
[16] E. Hertz, A. Rouzée, S. Guérin, B. Lavorel, and O. Faucher, Phys. Rev. A **75**, 031403(R) (2007).
[17] K. Nakagami, Y. Mizumoto, and Y. Ohtsuki, J. Chem. Phys. **129**, 194103 (2008).
[18] A. Rouzée, S. Guérin, O. Faucher, and B. Lavorel, Phys. Rev. A **77**, 043412 (2008).
[19] T. Suzuki, Y. Sugawara, S. Minemoto, and H. Sakai, Phys. Rev. Lett. **100**, 033603 (2008).
[20] J. P. Cryan, P. H. Bucksbaum, and R. N. Coffee, Phys. Rev. A **80**, 063412 (2009).
[21] S. Pabst and R. Santra, Phys. Rev. A **81**, 065401 (2010); **82**, 049901(E) (2010).
[22] M. Artamonov and T. Seideman, Phys. Rev. A **82**, 023413 (2010).
[23] M. Lapert, S. Guérin, and D. Sugny, Phys. Rev. A **83**, 013403 (2011).
[24] H. Abe and Y. Ohtsuki, Phys. Rev. A **83**, 053410 (2011).
[25] M. Z. Hoque, M. Lapert, E. Hertz, F. Billard, D. Sugny, B. Lavorel, and O. Faucher, Phys. Rev. A **84**, 013409 (2011).
[26] S. Zhang, C. Lu, J. Shi, T. Jia, Z. Wang, and Z. Sun, Phys. Rev. A **84**, 013408 (2011).
[27] D. Baek, H. Hasegawa, and Y. Ohshima, J. Chem. Phys. **134**, 224302 (2011).
[28] H. Abe and Y. Ohtsuki, Chem. Phys. **400**, 13 (2012).
[29] J. Itatani, J. Levesque, D. Zeidler, H. Niikura, H. Pepin, J. C. Kieffer, P. B. Corkum, and D. P. Villeneuve, Nature **432**, 867 (2004).
[30] C. Vozzi, M. Negro, F. Calegari, G. Sansone, M. Nisoli, S. De Silvestri, and S. Stagira, Nat. Phys. **7**, 822 (2011).
[31] B. M. McFarland, J. P. Farrell, P. H. Bucksbaum, and M. Gühr, Science **322**, 1232 (2008).
[32] P. Hockett, C. Z. Bisgaard, O. J. Clarkin, and A. Stolow, Nat. Phys. **7**, 612 (2011).
[33] S. Fleischer, I. Sh. Averbukh, and Y. Prior, Phys. Rev. A **74**, 041403(R) (2006).
[34] S. Fleischer, I. Sh. Averbukh, and Y. Prior, Phys. Rev. Lett. **99**, 093002 (2007).
[35] H. Akagi, T. Kasajima, T. Kumada, R. Itakura, A. Yokoyama, H. Hasegawa, and Y. Ohshima, Appl. Phys. B **109**, 75 (2012).
[36] B. L. Yoder, R. Bisson, P. M. Hundt, and R. D. Beck, J. Chem. Phys. **135**, 224703 (2011).
[37] Y. Khodorkovsky, J. R. Manson, and I. Sh. Averbukh, Phys. Rev. A **84**, 053420 (2011).
[38] Z. Ning and J. C. Polanyi, J. Chem. Phys. **137**, 091706 (2012).
[39] T. Kanai and H. Sakai, J. Chem. Phys. **115**, 5492 (2001).
[40] R. Tehini and D. Sugny, Phys. Rev. A **77**, 023407 (2008).
[41] M. Lapert, R. Tehini, G. Turinici, and D. Sugny, Phys. Rev. A **78**, 023408 (2008).
[42] S. De, I. Znakovskaya, D. Ray, F. Anis, N. G. Johnson, I. A. Bocharova, M. Magrakvelidze, B. D. Esry, C. L. Cocke, I. V. Litvinyuk, and M. F. Kling, Phys. Rev. Lett. **103**, 153002 (2009).
[43] K. Oda, M. Hita, S. Minemoto, and H. Sakai, Phys. Rev. Lett. **104**, 213901 (2010).
[44] H. Yun, H. T. Kim, C. M. Kim, C. H. Nam, and J. Lee, Phys. Rev. A **84**, 065401 (2011).
[45] K. Nakajima, H. Abe, and Y. Ohtsuki, J. Phys. Chem. A **116**, 11219 (2012).
[46] M. Spanner, S. Patchkovskii, E. Frumker, and P. Corkum, Phys. Rev. Lett. **109**, 113001 (2012).
[47] C. Qin, Y. Liu, A. Zhang, and Y. Liu, Eur. Phys. J. D **68**, 108 (2014).
[48] D. Sugny, A. Keller, O. Atabek, D. Daems, C. M. Dion, S. Guérin, and H. R. Jauslin, Phys. Rev. A **69**, 033402 (2004).
[49] S. Fleischer, Y. Zhou, R. W. Field, and K. A. Nelson, Phys. Rev. Lett. **107**, 163603 (2011).
[50] S. Fleischer, R. W. Field, and K. A. Nelson, Phys. Rev. Lett. **109**, 123603 (2012).
[51] S.-L. Liao, T.-S. Ho, H. Rabitz, and S.-I Chu, Phys. Rev. A **87**, 013429 (2013).
[52] J. Ortigoso, J. Chem. Phys. **137**, 044303 (2012).
[53] Z.-Y. Zhao, Y.-C. Han, Y. Huang, and S.-L. Cong, J. Chem. Phys. **139**, 044305 (2013).
[54] D. Daranciang, J. Goodfellow, M. Fuchs, H. Wen, S. Ghimire, D. A. Reis, H. Loos, A. S. Fisher, and A. M. Lindenberg, Appl. Phys. Lett. **99**, 141117 (2011).

[55] A. Goban, S. Minemoto, and H. Sakai, Phys. Rev. Lett. **101**, 013001 (2008).
[56] O. Ghafur, A. Rouzée, A. Gijsbertsen, W. K. Siu, S. Stotle, and M. J. J. Vrakking, Nat. Phys. **5**, 289 (2009).
[57] L. Holmegaard, J. H. Nielsen, I. Nevo, H. Stapelfeldt, F. Filsinger, J. Küpper, and G. Meijer, Phys. Rev. Lett. **102**, 023001 (2009).
[58] D. Daems, S. Guérin, D. Sugny, and H. R. Jauslin, Phys. Rev. Lett. **94**, 153003 (2005).
[59] E. Gershnabel, I. Sh. Averbukh, and R. J. Gordon, Phys. Rev. A **74**, 053414 (2006).
[60] K. Kitano, N. Ishii, and J. Itatani, Phys. Rev. A **84**, 053408 (2011).
[61] C.-C. Shu and N. E. Henriksen, Phys. Rev. A **87**, 013408 (2013).
[62] I. I. Boradjiev and N. V. Vitanov, Phys. Rev. A **88**, 013402 (2013).
[63] Y. Huang, T. Xie, J. Li, J. Yu, and S.-L. Cong, Laser Phys. **24**, 016002 (2014).
[64] Y. Ohtsuki and K. Nakagami, Phys. Rev. A **77**, 033414 (2008).
[65] A. P. Peirce, M. A. Dahleh, and H. Rabitz, Phys. Rev. A **37**, 4950 (1988).
[66] R. Kosloff, S. A. Rice, P. Gaspard, S. Tersigni, and D. J. Tannor, Chem. Phys. **139**, 201 (1989).
[67] G. J. Maroulis, J. Phys. Chem. **100**, 13466 (1996).